Residual Strain Analysis in Linear Friction Welds of Similar and Dissimilar Titanium Alloys Using Energy Dispersive X-ray Diffraction



RITWIK BANDYOPADHYAY, JOHN ROTELLA, DIWAKAR NARAGANI, JUN-SANG PARK, MICHAEL EFF, and MICHAEL D. SANGID

Residual strains in linear friction welds (LFW) of similar, Ti-6Al-4V (Ti64) welded to Ti-6Al-4V, and dissimilar, Ti-6Al-4V welded to Ti-5Al-5V-5Mo-3Cr (Ti5553), titanium alloys have been characterized using energy-dispersive X-ray diffraction. For each type of LFW, one sample was chosen in the as-welded (AW) condition and another sample was selected after a post-weld heat treatment (HT). In the present work, residual strains have been separately studied in the alpha and beta phases of the material, and five components (three axial and two shear) have been reported in each case. In-plane axial components of the residual strains show a smooth and symmetric behavior about the weld center for the Ti64-Ti64 LFW samples in the AW condition, whereas these components in the Ti64-Ti5553 LFW sample show a symmetric trend with jump discontinuities. Such jump discontinuities, observed in both the AW and HT conditions of the Ti64-Ti5553 samples, suggest different strain-free lattice parameters in the weld region and the parent material, whereas the results from the Ti64-Ti64 LFW samples in both AW and HT conditions suggest nearly uniform strain-free lattice parameters throughout the weld region. Finally, the observed trends in the in-plane axial residual strain components have been rationalized by the corresponding microstructural changes and variations across the weld region via backscatter electron (BSE) images.

https://doi.org/10.1007/s11661-018-5034-0 © The Minerals, Metals & Materials Society and ASM International 2018

I. INTRODUCTION

LINEAR friction welding (LFW) is commonly used in the aerospace industry to produce cost-effective and high-quality welds in components made from titanium (Ti) alloys, such as bladed discs or blisks. One of the benefits of the LFW process is joining dissimilar materials, thereby allowing components to possess location-specific properties. During the welding process, one reciprocating surface is brought into contact with a stationary surface at high frequency under applied load. This results in a steep temperature gradient across the

RITWIK BANDYOPADHYAY and DIWAKAR NARAGANI are with the School of Aeronautics and Astronautics, Purdue University, West Lafayette, IN 47907. JOHN ROTELLA is with the School of Materials Engineering, Purdue University, West Lafayette, IN 47907. JUN-SANG PARK is with the Advanced Photon Source, Argonne National Laboratory, Lemont, IL 60439. MICHAEL EFF is with the Edison Welding Institute, 1250 Arthur E. Adams Dr., Columbus, OH 43221. MICHAEL D. SANGID is with the School of Aeronautics and Astronautics, Purdue University and also with the the School of Materials Engineering, Purdue University. Contact e-mail: msangid@purdue.edu.

Manuscript submitted June 6, 2018.

Published online: 06 December 2018

weld interface. Such localized heating along with microstructural variations and poor thermal conductivity of Ti alloys results in highly localized residual stresses in the weld region. [1–3] The role of residual stress in the failure of engineering component is well recognized. [4] Therefore, it is necessary to provide a detailed characterization of the residual stress present in LFW joints of similar and dissimilar Ti alloys.

Residual stress distributions can be characterized using a wide range of techniques. [5] In particular, diffraction-based techniques using X-rays or neutron beam measure the inter-planar spacing, which is used to compute the lattice strains. These lattice strain measurements coupled with appropriate constitutive relationships provide information regarding the residual stress in the material. [6] Energy-dispersive X-ray diffraction (EDD) method has been used to quantify the residual stresses in engineering components in the past. [7–11] This method is particularly attractive because (i) high energy X-rays can penetrate tens of millimeters of typical engineering alloys, (ii) the incident X-ray beam can be reduced to offer sub-mm spatial resolution in the directions perpendicular to the beam in a typical setup, and (iii) acquisition time is relatively short. These characteristics enable spatial mapping of residual strain

in an engineering component. Additionally, the sample can be manipulated to measure the strains along multiple directions to determine the strain tensor (and thereby stress tensor).

There are a few studies available in literature characterizing the residual stress distributions in the LFW joints of Ti alloys. [12–16] Most of the works involve welds of similar Ti alloys [12–15] and only one work considers dissimilar Ti alloys.^[16] Daymond and Bonner measured the residual strains in the LFW joint of Ti-6Al-4V of different grades using pulsed neutron diffraction method. [12] Preuss et al. did a similar study on as-welded and heat-treated samples of IMI550 (Ti-4Al-2Sn-4-Mo-0.5Si).[13] Romero et al. studied the effect of forging pressure on the microstructural features and residual stresses in the LFW joint of Ti-6Al-4V. [14] Frankel et al. did a comparative study on the residual stress distribution in two similar LFW joints made of Ti-6Al-4V and Ti-6Al-2Sn-4Zr-2Mo. [15] Unlike the aforementioned works, Xie et al. studied residual stresses in welds composed of two dissimilar Ti-5Al-2Sn-2Zr-4Mo-4Cr (Ti17) alloys, namely, β Ti17 and $\alpha + \beta$ Ti17. [16]

The previously mentioned works, related to LFW of Ti alloys, [12-16] considered either in-plane components or three axial components of stress/strain for only the α phase in the Ti alloy. These studies emphasized that corrections should be made to the strain-free lattice parameter as a function of the distance from the weld center for an accurate description of the residual stress/strain and concluded that tensile stresses predominantly exist in the weld region. [12-16] Although residual stress/strain distributions are found to be symmetric about the center of the weld for similar Ti alloys, [12,14,15] the reported distributions of residual stress/strain in the welds of dissimilar alloys are not, strictly speaking, symmetric. [16]

In the present work, residual strains in the LFW joints of similar (Ti-6Al-4V welded to Ti-6Al-4V) and dissimilar (Ti-6Al-4V welded to Ti-5Al-5V-5Mo-3Cr) Ti alloys are studied using the EDD method considering both α and β phases. As opposed to the existing literature, five components of the residual strain tensor are reported (three axial and two shear). Comparative studies for similar and dissimilar welds are presented. Further, observed trends in the in-plane axial components of the residual strains are explained and supported by microstructural changes and variations across the weld interface via backscatter electron (BSE) images. In the present study, the residual strain data are presented, as opposed to residual stresses, based on uncertainty in the

elastic modulus, especially for the dissimilar LFWs. Additionally, the strain-free lattice parameter is taken as constant over the weld region, which is a simplification. It is the intention of the present paper to focus on the *tensorial* description of the residual strain and the corresponding micrographs. The data are presented with minimal modifications to allow further researchers to apply gradients in the elastic modulus or strain-free lattice parameter.

The paper is organized as follows. Section II illustrates the weld materials, parameters, and electron microscopy (EM) characterization technique. Section III describes the energy-dispersive X-ray diffraction method and post-processing methodologies to obtain the residual strains. The residual strain results are reported in Section IV. Observed trends in the in-plane axial components of the residual strains are discussed and explained via BSE images in Section V. Finally, concluding remarks are drawn in Section VI.

II. MATERIALS AND METHODOLOGY

A. Materials

In this study, several Ti alloys and combinations were selected for LFW, as shown in Table I. For the first set of samples where two similar Ti alloys were joined by LFW, two pieces of Ti-6Al-4V alloy, denoted as Ti64 from here on, in α - β processed state were used. The α phase has a hexagonal close-packed (HCP) structure and the β phase has a body-centered cubic (BCC) structure. For the second set of samples where two dissimilar Ti alloys were joined by LFW, Ti-5Al-5V-5-Mo-3Cr, denoted as Ti5553 from here on, is used in the oscillating side and Ti64 in mill-annealed state is used in the fixed side. The material with the greater flow stress at the evaluated temperature was selected for the oscillating component in the dissimilar weld because a rigid oscillating component reduces unwanted deformation of the component during welding and generally leads to better weld quality. The difference between the two Ti64 variants is the morphology and volume fraction of the β phase.

B. Weld Parameters and Heat Treatment

Each set of material welding parameters underwent iterative development trials and parameter selection based upon previous welding trials at the Edison Welding Institute. Each weld's quality was assessed

Table I. Material for Welded Components

Material Combination	Oscillating Side Material	Starting Microstructure of Oscillating Component	Fixed Side Material	Starting Microstructure of Fixed Component
Ti64-Ti64	Ti64	α - β processed: received in mill-annealed condition per AMS 4911 ^[17] followed by annealing at 704 °C for 2 h	Ti64	α–β processed: received in mill-annealed condition per AMS 4911 ^[17] followed by annealing at 704 °C for 2 h
Ti64-Ti5553	Ti5553	Solution treated at 838 °C for 2 h and aged at 593 °C for 8 h	Ti64	Mill-annealed per AMS 4911 ^[17]

All heat treatments were followed by air cooling.

based upon flash curl, weld time, process forces, visual inspection, and a quick rudimentary pull test to assess ultimate tensile strength. The pull test was used as a qualitative measure, and formal tensile testing was conducted on select welds. The welds characterized in this study represent the best or near best case welding conditions from the parameter development trials.

The weld is split into three distinct stages: scrub, weld, and forge. The scrub allows the oscillator to reach amplitude at the desired frequency under low load and can be used to build heat into the part. The scrub time and pressure (*i.e.*, pressure applied at the beginning of oscillation) were 0.2 seconds and 22.8 MPa, respectively. The weld phase uses oscillation amplitude, frequency, and pressure of the moving component to deform the material and create a solid state joint. Afterwards, oscillation is stopped and a forge pressure equal to or greater than the weld pressure is applied during the forge phase and held for a short duration (*i.e.*, forge time). The linear friction weld parameters for each weld are summarized in Table II.

Two weld samples using Ti64-Ti64 combination and two samples using Ti64-Ti5553 combination were fabricated using the LFW parameters listed in Table II. One sample for each combination was set aside and these are designated as the as-welded (AW) condition. The remaining samples underwent a post-weld heat treatment and are referred to as HT samples throughout this paper. The Ti64-Ti64 sample was heat treated at 704 °C for 2 hours followed by air cooling. Similarly, the Ti64-Ti5553 sample was heat treated below the β solvus temperature of Ti5553.

C. Electron Microscopy Characterization

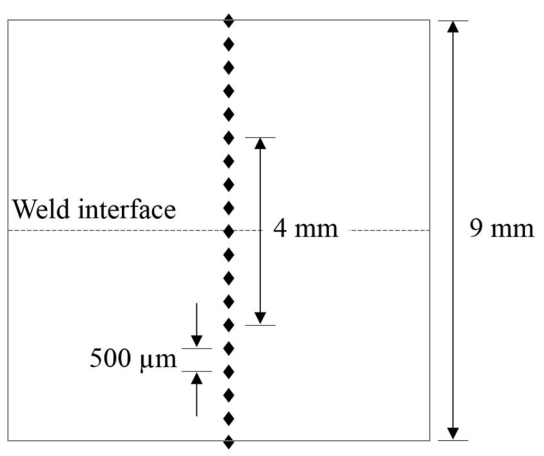
All sample pedigrees were characterized on an FEI Quanta 3D FEG Dual-beam SEM with a four-quadrant BSE detector. The BSE detector was used in Z-contrast mode; all four quadrants had a positive bias. Specimens were mechanically ground and polished using $0.3 \mu m$ alumina suspension. The final polish was achieved by using vibratory polishing with a suspension of 0.05 μ m colloidal silica. Specimens were marked perpendicular to the weld interface of the joined materials. Indents were placed every 500 μ m across the 9 mm weld region, 4.5 mm on each side of the weld, and used for spatial positioning during BSE characterization (see Figure 1). Images were taken along the fiducially marked path, continuously 2 mm from the weld in both directions and every 500 μ m after that, until 4.5 mm was imaged on each side of the weld. This imaging scheme was use to

capture the microstructural transitions close to the weld and the microstructure further away from the weld.

III. RESIDUAL STRAIN MEASUREMENT

A. Energy-Dispersive X-ray Diffraction Experiment

Figure 2 shows the setup for the EDD experiment at the 6-BM-A endstation of the Advanced Photon Source (APS), Argonne National Laboratory. Figure 3 shows a schematic view of the setup and Figure 4 illustrates the geometry in 2D view. In this schematic, the X-Y-Zcoordinate system is fixed in the lab. Slits 1-3 controlled the size of the incoming polychromatic X-ray beam. A set of filters removed the low energy photons that were not useful for strain measurements in this sample. Slits 4-5 and 6-7 were associated with the vertical and horizontal detectors, respectively, and controlled the sizes of the gage volumes interrogated by the detectors. Two germanium detectors were placed approximately 1 m away from the gage volume—one on the Y–Z plane and the other on the X-Z plane. The detector placed on the Y-Z plane is referred to as the vertical detector and q_v is the corresponding scattering vector associated with the strain measurement direction. The detector placed on the X-Z plane is referred to as the horizontal detector and q_h is the corresponding scattering vector.



◆ Fiducial marks for BSE imaging

Fig. 1—Schematic of the weld region showing fiducial marks for BSE imaging. Images were taken along the fiducially marked path, continuously 2 mm from the weld in both directions and every $500~\mu m$ after that.

Table II. Linear Friction Weld Parameters Used to Fabricate the Weld Samples

Material Combination	Frequency (Hz)	Amplitude (mm)	Weld Pressure (MPa)	Programmed Burn-off (mm)	Forge Pressure (MPa)	Forge Time (s)	Measured Upset (mm)
Ti64-Ti64	35	2.5	100	2.48	100	5	3.51
Ti64-Ti5553	45	1.1	172.4	3.18	172.4	5	N/A

The programmed burn-off is defined as the displacement of the weld platen. The upset is the total loss in length of the joined component after welding.

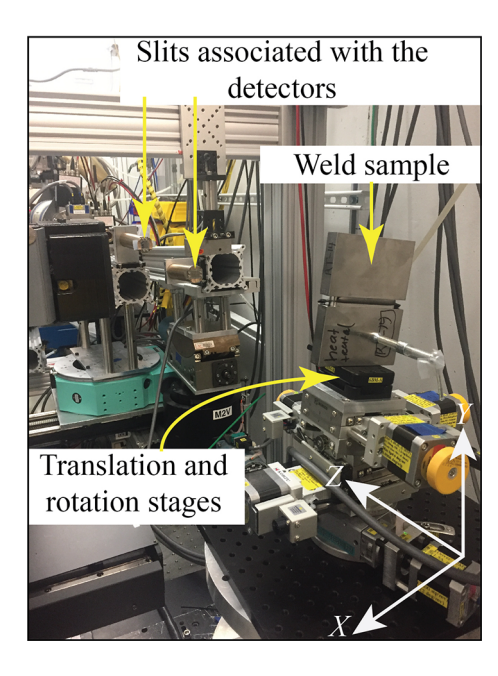


Fig. 2—The overall experimental setup for the EDD measurement.

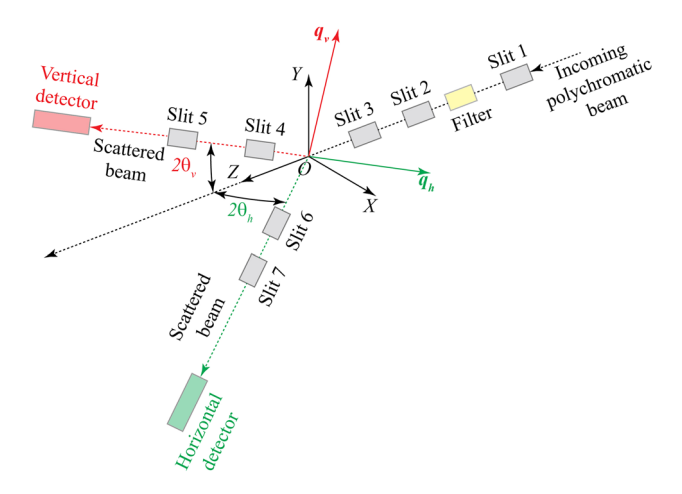


Fig. 3—A schematic of the experimental setup, in which the X–Y–Z coordinate system is fixed in the lab.

The vertical and horizontal detectors and associated slits were positioned such that $2\theta_{\nu}$ and $2\theta_{\rm h}$ were 5.00 and 4.90 deg, respectively. Furthermore, the slits were adjusted such that the gage volume viewed by the vertical detector and the gage volume viewed by the horizontal detector coincide. The centroid of the gage volume is denoted as O in Figures 3 and 4(a). Calibration of the setup using a thin CeO₂ powder sample indicated that the gage volume was approximately 5 mm long in the Z direction. The incoming beam size was 0.2 mm \times 0.2 mm defined by the upstream slits. At these slit settings and detector locations, the azimuthal coverage was approximately 1 deg for both detectors.

The goal of the EDD experiments is to obtain a strain tensor map in the weld region of a sample. Figure 5 illustrates how this goal was achieved. The sample was

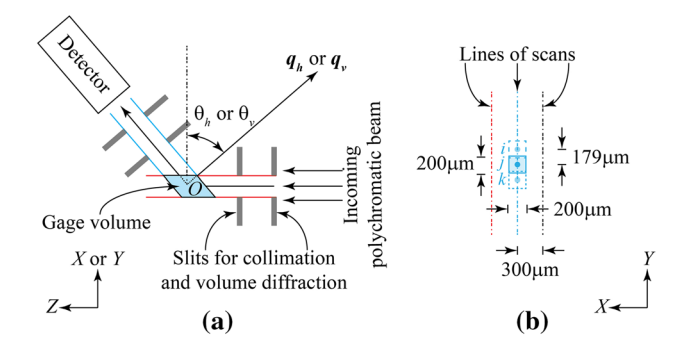


Fig. 4—(a) 2D schematic of the gage volume interrogated by a detector in the experimental setup. (b) The projection of the gage volume on the X-Y plane. For the residual strain characterization of each specimen, multiple line scans 300 μ m apart are taken. Experimentally obtained lattice strain at a 'point' is defined by the average value of the same over the illuminated gage volume, the centroid of which coincides with the 'point.' In the figure i,j,k represent three such consecutive 'points' and the overlap of the illuminated gage volume is shown.

positioned such that the sample mid-plane along 3, coincides with O. All the crystal planes in the sample that reside in the gage volume and satisfy the diffraction condition for q_v and q_h contribute to the spectra obtained by the vertical and horizontal detectors, respectively. Given the average grain size, we anticipate around 10⁵ grains to be in the gage volume. For a particular sample position $P(x_1, x_2, x_3)$, the sample was rotated by discrete values in Ω (rotation about the Y axis), while keeping Θ (rotation about the X axis) and γ (rotation about the Z axis) at 0 deg, and by discrete values in γ , while keeping Ω and Θ at 0 deg. The values of Ω were -45, 0, 15, 30, and 45 deg and the values of χ were -8, 0, and 8 deg. With these angular motions, seven measurements of lattice inter-planar spacings were obtained from each detector. Later, these measurements will be used to compute the components of the strain tensor. Rotation also implies that the crystals participating in diffraction is changing from one angle setting to the other even for the same sample position. In fact, because of the sample rotation, the spatial resolution attainable based on the size of slits for the incoming X-ray beam was compromised, most severely in the 1-direction. After the suite of rotations at a point P, the sample was translated along the Y axis to interrogate a series of points across the weld. For the Ti64-Ti64 LFW samples (AW and HT), three line scans along Y direction were performed with each line separated along the 1-axis by 0.3 mm (see Figure 4(b)). For the Ti64-Ti5553 LFW samples (AW and HT), two line scans were performed with lines separated by 0.3 mm. All line scans were nominally in the mid-section of the sample along 1- and 3-axes.

B. Data Post-Processing

Post-processing of the diffraction spectra involves two steps, namely, obtaining the lattice strains followed by peak fitting, and computing the components of the

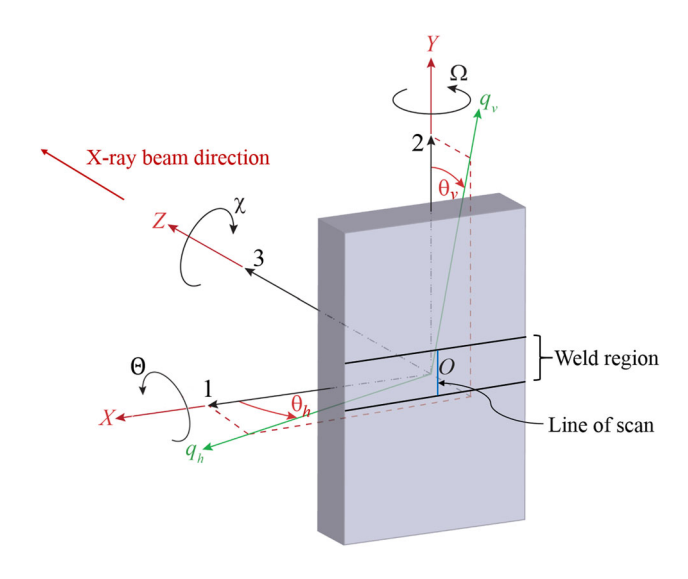


Fig. 5—A schematic of the linear friction weld part is shown. The 1-2-3 coordinate system is fixed to the sample and rotates with the sample.

residual strain tensor using the obtained lattice strains. First, the peak fitting and lattice strain measurement procedure will be outlined.

Figure 6 shows a representative diffraction pattern in the Ti64-Ti5553 HT LFW sample near the weld interface at $\Omega=0$ deg, $\chi=0$ deg. Each peak corresponds to a family of planes as described in Table III. The distortion of the lattice from its reference configuration may have both elastic and inelastic contributions. In the present work, the underlying assumption is that the shift of each peak along the horizontal axis is entirely due to the elastic contribution. The inelastic contributions can be investigated by studying peak aberrations^[18] or crystallographic structure changes^[19] but is beyond the scope of the present work.

The first, fourth, and fifth peaks for the α phase were well separated from other α and β peaks. Further, the fourth α peak was consistently present in all scanned locations and (Ω,χ) combinations for each LFW sample. Hence, the fourth α peak was fit using the pseudo-Voigt peak profile function in MATLAB. The fit was used to compute the lattice strain using

$$\varepsilon_{\mathbf{q_h}} = \frac{E_{\mathbf{h}}^{\mathbf{hkl}} - \frac{hc}{2d_0^{\mathbf{hkl}}\sin\theta_{\mathbf{h}}}}{\frac{hc}{2d_0^{\mathbf{hkl}}\sin\theta_{\mathbf{h}}}}$$
[1]

and

$$\varepsilon_{\mathbf{q}_{\mathbf{v}}} = \frac{E_{\mathbf{v}}^{\mathrm{hkl}} - \frac{hc}{2d_{0}^{\mathrm{hkl}}\sin\theta_{\mathbf{v}}}}{\frac{hc}{2d_{0}^{\mathrm{hkl}}\sin\theta_{\mathbf{v}}}},$$
 [2]

where ε_{q_h} and ε_{q_v} are lattice strains from horizontal and vertical detectors, respectively; E_h^{hkl} and E_v^{hkl} are fitted energy values for the peaks corresponding to $\{hkl\}$ planes from horizontal and vertical detectors, respectively; h is Planck's constant; c is speed of light in

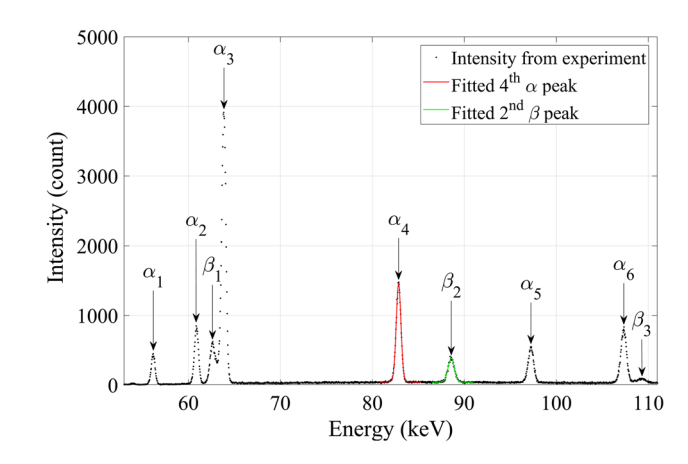


Fig. 6—The diffraction pattern from Ti64-Ti5553 HT sample near the weld interface obtained at $\Omega=0$ deg, $\chi=0$ deg configuration. In the plot, α_i represents *i*th peak corresponding to the α phase and β_i represents *i*th peak corresponding to the β phase. The first six α peaks correspond to the {100}, {002}, {101}, {102}, {110}, and {103} planes, respectively. The first three β peaks correspond to the {110}, {200}, and {211} planes, respectively.

vacuum; $d_0^{\rm hkl}$ is the reference inter-planar spacing corresponding to {hkl} planes.

Similarly, it can be seen that the second β peak is well isolated from other α and β peaks. Hence, the second β peak was chosen for peak fitting, and lattice strains were calculated using Eqs. [1] through [2]. Based on these peak choices, we are essentially using the α {110} and β {200} as strain gages embedded in the material.

For each measurement point, the residual strain tensors in the α and β phases were computed using the lattice strain values obtained above. For each Ω or χ , the lattice strains measured from the horizontal and vertical detectors can be related to the residual strain tensor as follows:

$$\boldsymbol{\varepsilon}_{\mathsf{q}_{\mathsf{h}}} = \boldsymbol{q}_{h} \boldsymbol{R} \boldsymbol{\varepsilon} \boldsymbol{R}^{\mathsf{T}} \boldsymbol{q}_{h}^{\mathsf{T}}, \tag{3}$$

$$\boldsymbol{\varepsilon}_{\mathbf{q}_{v}} = \boldsymbol{q}_{v} \boldsymbol{R} \boldsymbol{\varepsilon} \boldsymbol{R}^{\mathrm{T}} \boldsymbol{q}_{v}^{\mathrm{T}}, \tag{4}$$

where ε is the residual strain tensor in the 1-2-3 coordinate system; R is defined by

$$\mathbf{R}_{\Omega} = \begin{bmatrix} \cos \Omega & 0 & -\sin \Omega \\ 0 & 1 & 0 \\ \sin \Omega & 0 & \cos \Omega \end{bmatrix}$$
 [5]

or

$$\mathbf{R}_{\chi} = \begin{bmatrix} \cos \chi & -\sin \chi & 0\\ \sin \chi & \cos \chi & 0\\ 0 & 0 & 1 \end{bmatrix}$$
 [6]

depending on the sample rotation executed to measure the strain component.

At each (Ω,χ) combination, two equations exist, one from the horizontal detector and another from the vertical detector. Hence, an over-determined linear system can be formulated based on 14 equations and

Table III. Description of First Six α and β Peaks

Phase	First Peak	Second Peak	Third Peak	Fourth Peak	Fifth Peak	Sixth Peak
α	{100} {10 <u>1</u> 0}	{002} {0002}	{101} {10 <u>1</u> 1}	{102} {10 <u>1</u> 2}	{110} {1120}	{103} {1013}
β	{110}	{200}	{211}	{220}	{310}	{222}

In Fig. 6, only first three β peaks are seen. For the α phase, the three digit Miller indices are reported in the first row and the corresponding four digit Miller–Bravais indices are given in the second row.

six unknowns for each measurement point, which can be written as follows:

$$Ax = b, [7]$$

where

$$\mathbf{x} = [\varepsilon_{11}, \, \varepsilon_{22}, \, \varepsilon_{33}, \varepsilon_{12}, \, \varepsilon_{13}, \, \varepsilon_{23}]^{\mathrm{T}}$$
 [8]

$$\begin{split} \boldsymbol{b} = & \left[\varepsilon_{q_h}^{\Omega = -45\deg}, \varepsilon_{q_v}^{\Omega = -45\deg}, \varepsilon_{q_h}^{\Omega = 0\deg}, \varepsilon_{q_v}^{\Omega = 0\deg}, \\ & \varepsilon_{q_h}^{\Omega = 15\deg}, \varepsilon_{q_v}^{\Omega = 15\deg}, \varepsilon_{q_h}^{\Omega = 30\deg}, \varepsilon_{q_v}^{\Omega = 30\deg}, \\ & \varepsilon_{q_h}^{\Omega = 45\deg}, \varepsilon_{q_v}^{\Omega = 45\deg}, \varepsilon_{q_h}^{2 = -8\deg}, \varepsilon_{q_v}^{2 = -8\deg}, \varepsilon_{q_v}^{2 = -8\deg}, \\ & \varepsilon_{q_h}^{\chi = 8\deg}, \varepsilon_{q_v}^{\chi = 8\deg} \right]^T \end{split}$$

and the 14×6 coefficient matrix, A, depends on the seven configurations defined by the associated angles, $\Omega, \chi, \theta_h, \theta_v$. It should be noted that the coefficient matrix A is the same at all measurement point, whereas the b changes from point to point. Such a system is solved in MATLAB using a least square method wherein the L^2 norm of the residual, e = Ax - b, is minimized to determine the residual strain tensor. The above procedure is repeated at all points for each line scan for all LFW samples to find the components of the residual strain tensor. In the following section, we report the results from the MATLAB analysis.

IV. RESIDUAL STRAIN RESULTS

The strain-free lattice parameters for both the α and β phases were determined using the Ti64-Ti64 HT sample. The lattice parameters were adjusted so that the lattice strains obtained after peak fitting (considering the fourth peak of the α phase and the second peak of the β phase) from both detectors at all points on a line scan are minimized in an absolute sense. The results are a=2.931 Å, c=4.660 Å for the α phase and $\alpha=3.213$ Å for the β phase. These numbers are consistent with the reported range of values in the literature. Subsequently, these lattice parameters were used to compute lattice strains in all LFW samples.

The numerical accuracy depends on the error associated with the lattice strains and the least squares solution. For a powder material, typical strain uncertainty of the experimental setup at the 6-BM-A EDD setup is approximately 1×10^{-4} . The least squares solution of the over-determined linear system, Ax = b,

is same as the solution of the square system $A^{T}Ax = A^{T}b$. Therefore, the condition number* of $A^{T}A$ is

*If the condition number of the coefficient matrix of a linear system is very large (\gg 1), it is practically singular. Hence, the solution of the linear system is prone to large numerical error.

computed as a measure of the quality of the inverse operator, $(A^TA)^{-1}$. If all configurations and the associated angles (*i.e.*, Ω , χ , θ_{ν} , θ_{h}) are considered, the condition number of A^TA is 6962.6. If small angles θ_{ν} , θ_{h} are neglected (*i.e.*, set $\theta_{\nu} = 0 \deg, \theta_{h} = 0 \deg$), the condition number becomes 22.8. Further, if two configurations associated with the small angle χ are neglected (*i.e.*, neglect $\chi = 8 \deg, -8 \deg$ and set $\chi = 0 \deg$), the condition number becomes 14.4**. Therefore, it is evident

**It is to be noted, when θ_{ν} , θ_{h} or χ are neglected, a few columns of \boldsymbol{A} matrix only contain zeros. Those columns are neglected while calculating condition number.

that the small angles for θ_v , θ_h result in a bad quality or unreliable inverse operation, whereas the configurations defined by small angle χ do not affect the inversion operation significantly. If θ_v , θ_h are set to 0 deg, the information related to ε_{23} component of the residual strain tensor is lost but the rest of the components can be captured with higher confidence. The variations of the residual strain tensor components (except ε_{23}) in the α and β phases, across the weld region of all LFW samples, are shown in Figures 7 through 10.

It is shown in Figures 7 through 10 that shear strain components $(\varepsilon_{12}, \varepsilon_{13})$ are either near zero for HT condition or very small compared to normal components $(\varepsilon_{11}, \varepsilon_{22}, \varepsilon_{33})$ in the AW condition. Moreover, the rubbing action during the welding process took place on the 1–2 plane. Therefore, it can be reasonably assumed that the ε_{23} will be very small for all the cases. In the next section, the trends observed in the in-plane axial components $(\varepsilon_{11}, \varepsilon_{22})$ are described and explained using micrographs obtained through BSE images.

V. DISCUSSION

BSE imaging is used to evaluate the microstructure across the weld region and correlate the varying microstructures to the residual strain measurements,

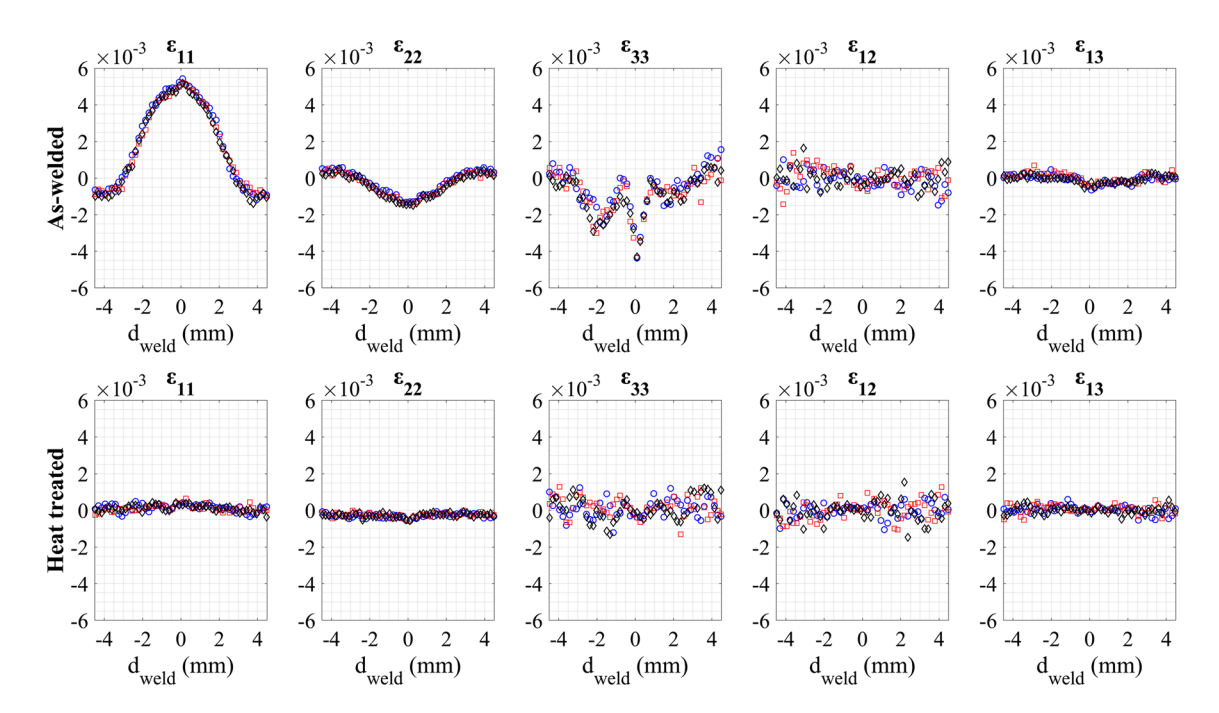


Fig. 7—Residual strain components in the as-welded and heat-treated joints of Ti64-Ti64 LFW sample are shown. These are obtained from fitting the $\{110\}$ peak of the α phase. Different markers in the plots correspond to different line scans across the weld.

Table IV. Grain Size Measurements of Different α Grain Structures in the Ti64-Ti64 AW Sample

	Ti64-Ti64 AW				
	Distance from Weld	0 mm	1.5 mm	3.0 mm	4.5 mm
α Grain Size (μm)	Basket-weave thickness Lamellar thickness Globular	$0.376 \pm 0.09 \ N/A \ N/A$	N/A N/A 13.26 ± 5.1	N/A N/A 14.08 ± 6.4	N/A N/A 10.94 ± 5.5

The thickness or width of the basket-weave and lamellar structures are reported, and the average grain size of the globular α is reported using the line-intercept method to measure grain size. Lamellar alpha grains were not detected/measured.

specifically ε_{11} and ε_{22} . If not stated explicitly, 'strain' in the following discussions corresponds only to the ε_{11} and ε_{22} components. For all BSE microstructure images, the β phase appears as the light regions, whereas the α phase appears relatively darker.

A. Ti64-Ti64 LFW in the As-Welded Condition

The residual strain profiles in the α phase for Ti64-Ti64 AW sample show a symmetric and smooth behavior throughout the weld region (see Figure 7). In Figure 8, a similar trend is observed within the β phase except a discontinuity within approximately \pm 0.8 mm distance from the weld center (i.e., $d_{\rm weld}=0$). This discontinuity is attributed to the fact that the second peak corresponding to the β phase was missing during the peak fitting process. The absence of the second β peak, which is well isolated from other α and β peaks, could be the result of a lack of β phase resulting from the welding process.

Figure 11(a) is a schematic showing the spatial position in which the micrographs are acquired on the Ti64-Ti64

AW sample. The region immediately adjacent to the weld displays a variable microstructure with increasing grain size and equiaxed structure as the distance from the weld region is increased along the 2 direction, as shown in Figures 11(b) and (c). The variable grain morphology shown in Figure 11(c) is consistent with the steep gradient of the measured residual strain, in both α and β phases, close to the weld interface. As summarized in Table IV, the fine basket-weave structures were observed in close proximity to the weld due to the rapid cooling after the LFW process. Further from the weld interface, 1.5 mm or more, only globular α grains were observed. Figures 11(d) and (e) show the microstructures at 1 and 4.5 mm above the weld interface, respectively. Similarly, Figures 11(f) and (g) show the microstructures at 1 and 4.5 mm below the weld region. It should be noted that the microstructure remains unchanged when comparing the micrographs from 1 and 4.5 mm away from the weld region (both above and below) explaining the symmetric behavior in the plots.

The residual strain measured in the β phase is greater than that in the α phase as shown in Figures 7 and 8,

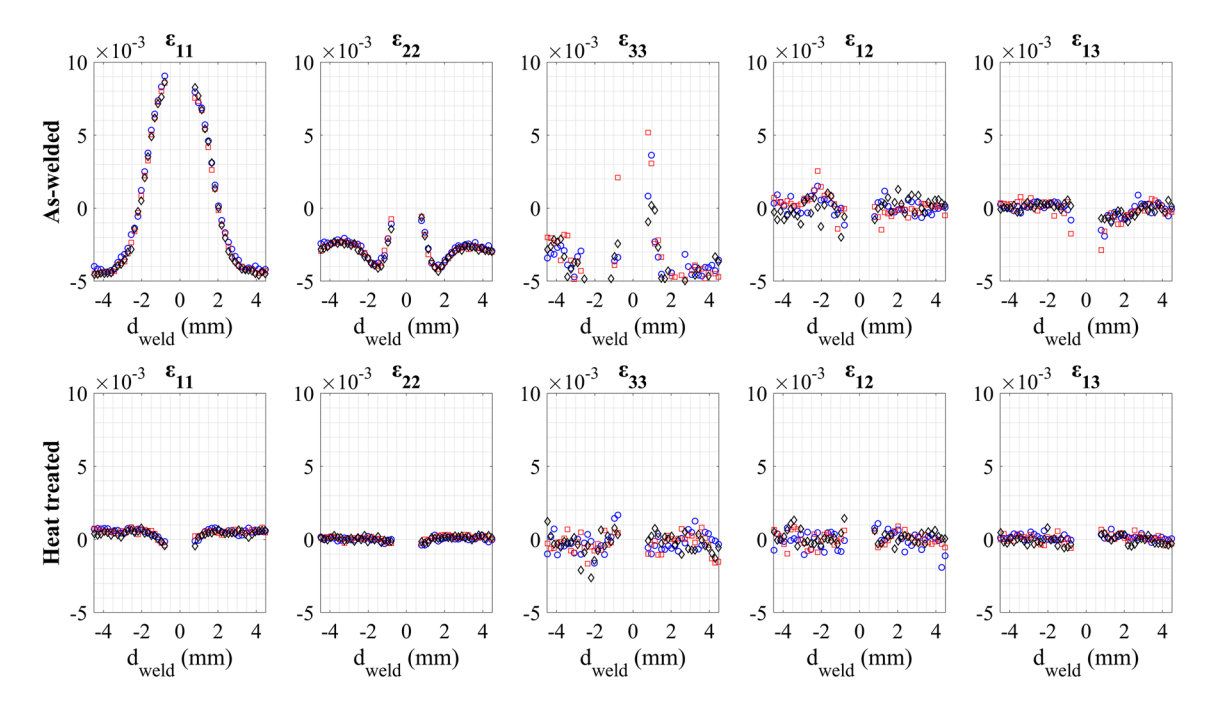


Fig. 8—Residual strain components in the as-welded and heat-treated joints of Ti64-Ti64 LFW sample are shown. These are obtained from fitting the 2nd peak of the β phase. Different markers in the plots correspond to different lines of scans.

Table V. Grain Size Measurements of Different α Grain Structures in the Ti64-Ti64 HT Sample

	Ti64-Ti64 HT					
	Distance from Weld	0 mm	1.5 mm	3.0 mm	4.5 mm	
α Grain size (μm)	Basket-weave thickness Lamellar thickness Globular	N/A 0.305 \pm 0.11 1.65 \pm 0.80	0.067 ± 0.01 N/A 9.62 ± 5.5	0.125 ± 0.03 N/A 8.90 ± 4.5	0.126 ± 0.03 N/A 11.06 ± 5.2	

The thickness or width of the basket-weave and lamellar structures are reported, and the average grain size of the globular α is reported using the line-intercept method to measure grain size.

where the β phase has peak strain measurements of 0.009 compared to the α phase maximum strain of 0.005in ε_{11} . The higher value of residual strain in the β phase could be attributed to the choice of the second β peak during the peak fitting process. It can be shown that the stiffness of the β phase along the {100} direction in a beta single crystal, associated with the second β peak, is much lower than the stiffness of the α phase along the $\{102\}$ direction, associated with the fourth α peak in uniaxial tension. For representative values of the elastic constants in the α and β phases, readers are referred to References 24 through 26; the procedure to calculate direction-dependent stiffness in cubic and hexagonal systems can be found in References 27, 28. Finally, ε_{11} is found to be greater than ε_{22} . This could be due to the fact that the specimen was oscillated along 1 direction during the welding process.

B. Ti64-Ti64 LFW in the Heat-Treated Condition

Residual strain profiles in the α phase of Ti64-Ti64 HT sample, as shown in Figure 7, show a flat and

smooth behavior throughout the weld area. A similar trend is observed in the β phase (see Figure 8). Similar to the Ti64-Ti64 AW sample, a discontinuity is seen in the β phase within approximately \pm 0.8 mm distance from the weld interface. Figure 12(a) is a schematic showing the spatial position of the micrographs for the Ti64-Ti64 HT sample. The region immediately adjacent to the interface displays a variable microstructure with increasing grain size as distance is increased from the weld interface along the 2 direction, as shown in Figures 12(b) and (c) and as summarized in Table V. In this case, the grains are fully recrystallized, even near the weld interface. This is supportive of the near-zero residual strain measured in both the α and β phases.

Figures 12(d) and (e) show the microstructures at 1 and 4.5 mm above the weld interface, respectively. Similarly, Figures 12(f) and (g) show the microstructure at 1 and 4.5 mm below the weld interface, respectively. The microstructure remains unchanged when comparing the micrographs from 1 and 4.5 mm away from the weld interface (both above and below). Unlike the as-welded condition, the heat-treated condition shows a very distinct weld interface, highlighted in Figure 12(h),

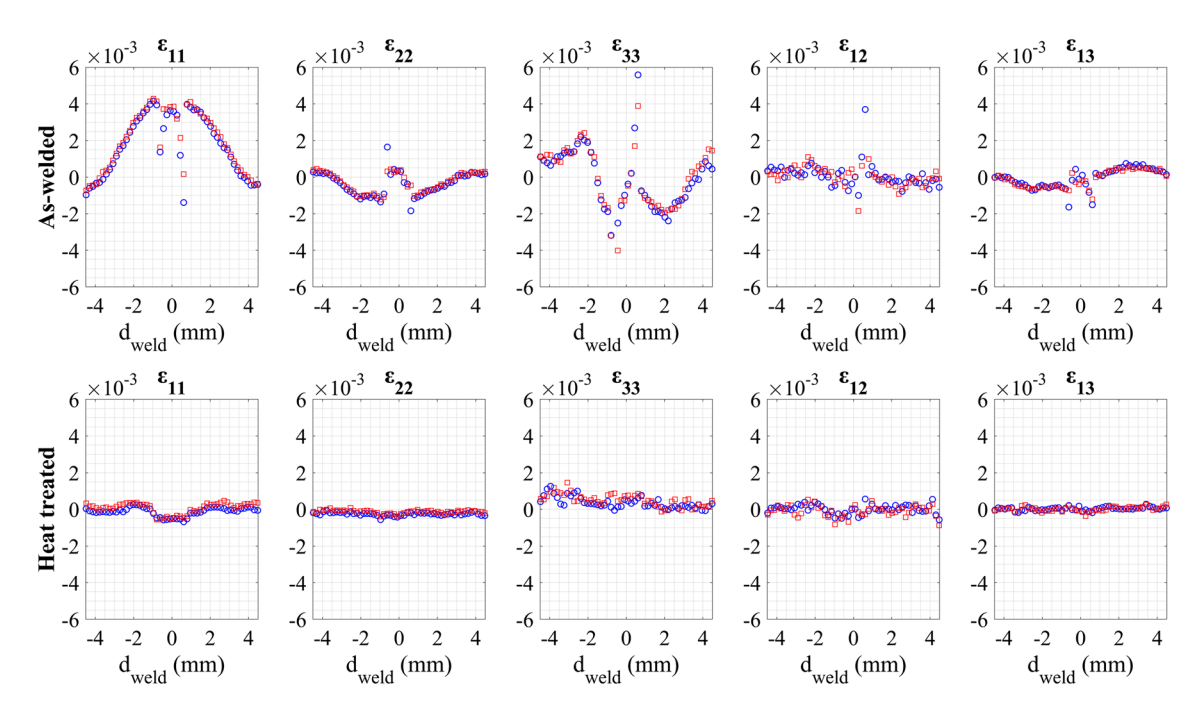


Fig. 9—Residual strain components in the as-welded and heat-treated joints of Ti64-Ti5553 LFW sample are shown. These are obtained from fitting the 4th peak of the α phase. In the figure, Ti64 is to the left and Ti5553 is to the right. Different markers in the plots correspond to different lines of scans.

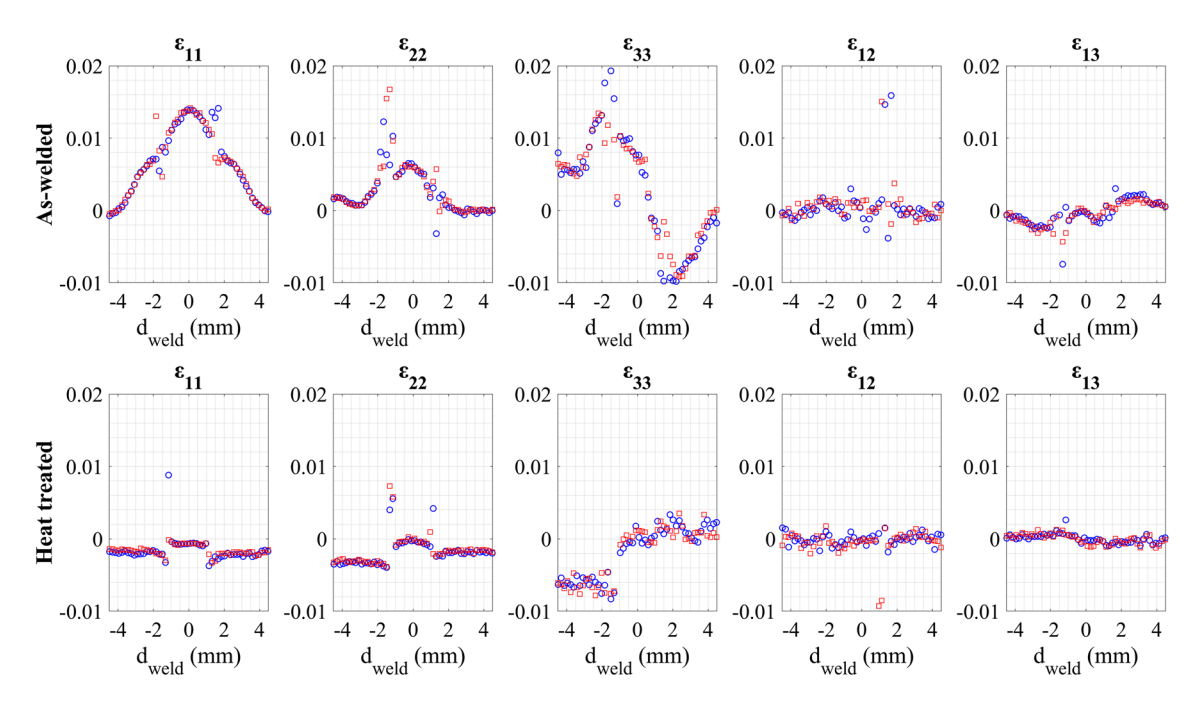


Fig. 10—Residual strain components in the as-welded and heat-treated joints of Ti64-Ti5553 LFW sample are shown. These are obtained from fitting the 2nd peak of the β phase. In the figure, Ti64 is to the left and Ti5553 is to the right. Different markers in the plots correspond to different lines of scans.

where small grains have formed parallel to axis 1. Three forms of α phase were present in this condition, namely, globular, lamellar, and basket-weave. Their sizes with respect to location from the weld interface are summarized in Table V.

C. Ti64-Ti5553 LFW in the As-Welded Condition

Residual strain profiles in the α phase of the Ti64-Ti5553 AW sample are shown in Figure 9. The strain profiles have a symmetric behavior throughout

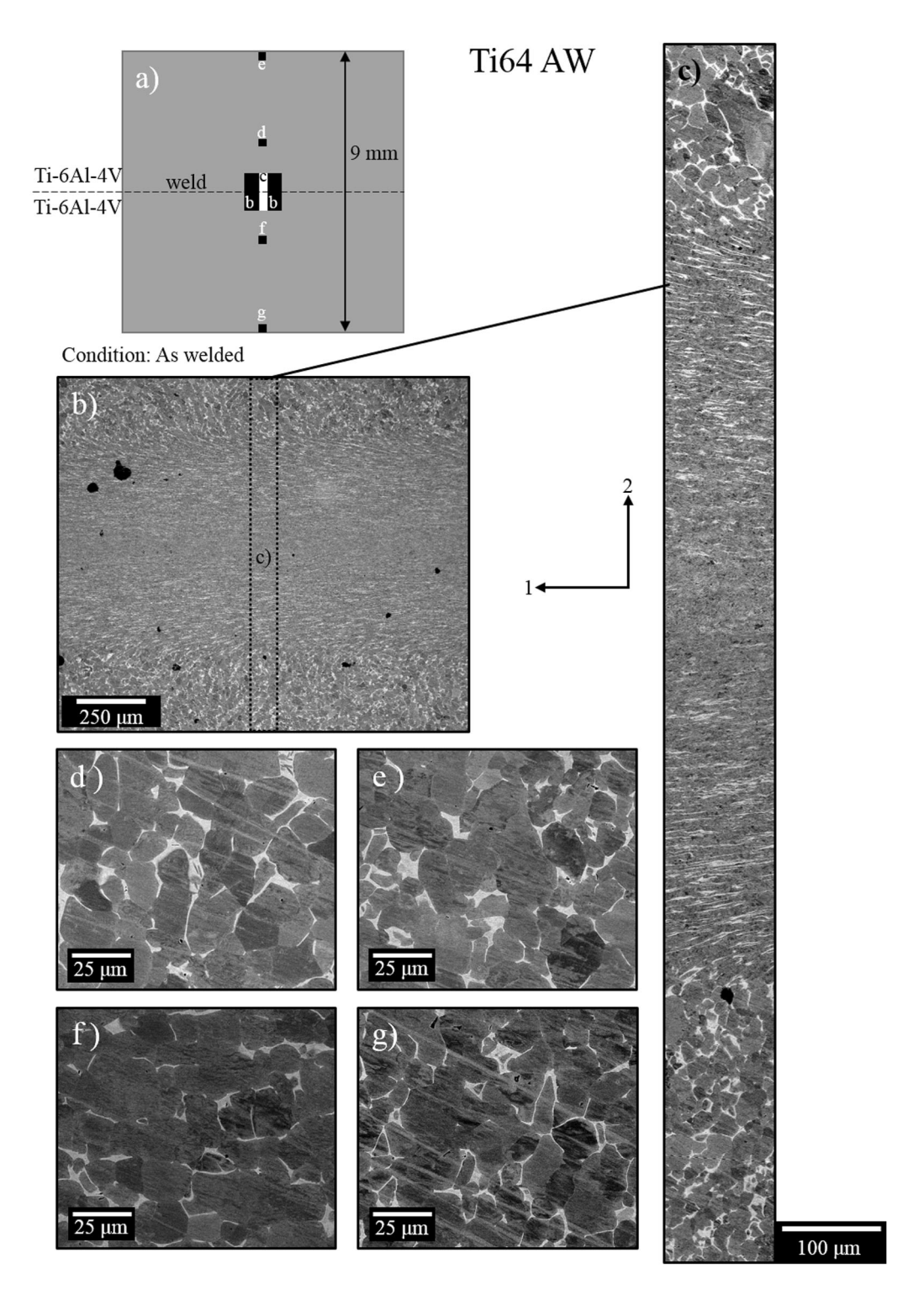


Fig. 11—Displays the Ti64-Ti64 sample in the as-welded condition: (a) A schematic representing the location of the following images, in relation to the weld area, (b) an overview of the weld area, (c) an enlarged region, 1.23 mm in height taken across the weld region, approximately 0.6 mm in each direction, (d) a field of view (FOV) 1.0 mm above the weld region, (e) a FOV 4.5 mm above the weld region, (f) a FOV 1 mm below the weld region, and (g) a FOV 4.5 mm below the weld region.

the weld area. A similar trend is observed in the β phase (see Figure 10). Strain profiles in both phases show jump discontinuities about 1 mm from both sides of the weld interface. Micrographs corresponding to this sample are shown in Figure 13. Figure 13(a) displays a schematic representing the locations of the micrograph

images on the sample. The jump discontinuities observed in strain measurements approximately 1 mm from the weld can be partly attributed to a change in microstructure at that point. Figure 13(d) shows an interface, on the Ti5553 side, that has formed where the microstructure abruptly changes. The top of this

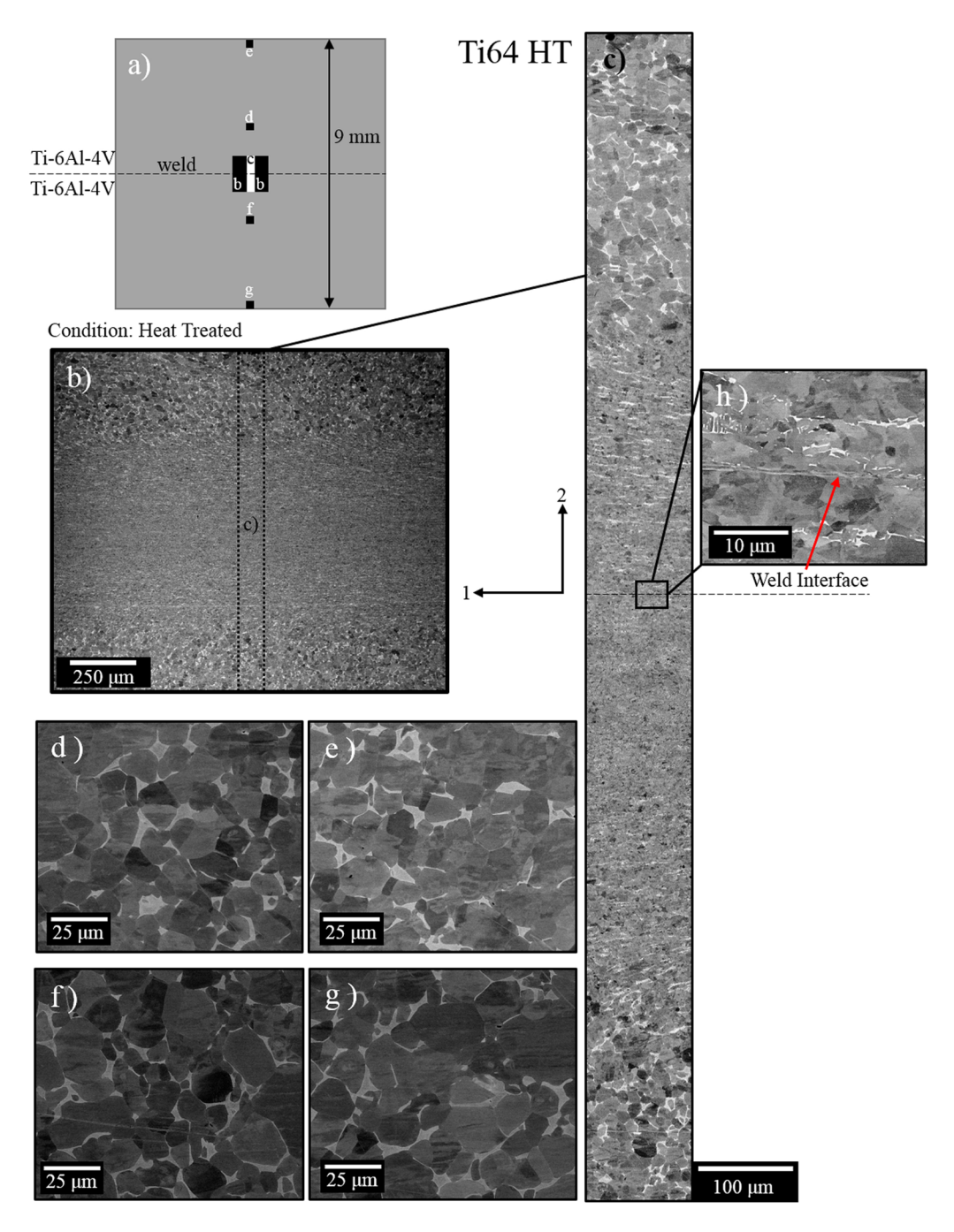


Fig. 12—Displays the Ti64-Ti64 sample in the heat-treated condition: (a) A schematic representing the location of the following images, in relation to the weld area, (b) an overview of the weld area, (c) an enlarged region, 1.23 mm in height taken across the weld region approximately 0.6 mm in each direction, (d) a FOV 1.0 mm above the weld region, (e) a FOV 4.5 mm above the weld region, (f) a FOV 1 mm below the weld region, (g) a FOV 4.5 mm below the weld region, (h) the weld interface created at the joining point of the two materials.

micrograph has even gray-scale intensity, but over this interface, as pointed out in Figure 13(d), a mix of dark and light areas in the BSE image are present. At these locations, there is a composition change, possibly responsible for the discontinuity in the data. At 4.5 mm away from the weld, the Ti5553 microstructure is more regular and indicative of the base material compared to the microstructure close to weld interface as shown in Figure 13(e). At the weld interface and on

the Ti5553 side, no agglomerates of the α phase are present in the BSE images. Similarly, the Ti64 side of the weld shows a discontinuity about 1 mm from the weld interface, this can be partly attributed to a transition from the presence of a fine basket-weave structure to a larger lamellar configuration of the α phase, in addition to the large globular grains as shown in Figure 13(f). These smaller basket-weave colonies that are present close to the weld transform completely to the larger

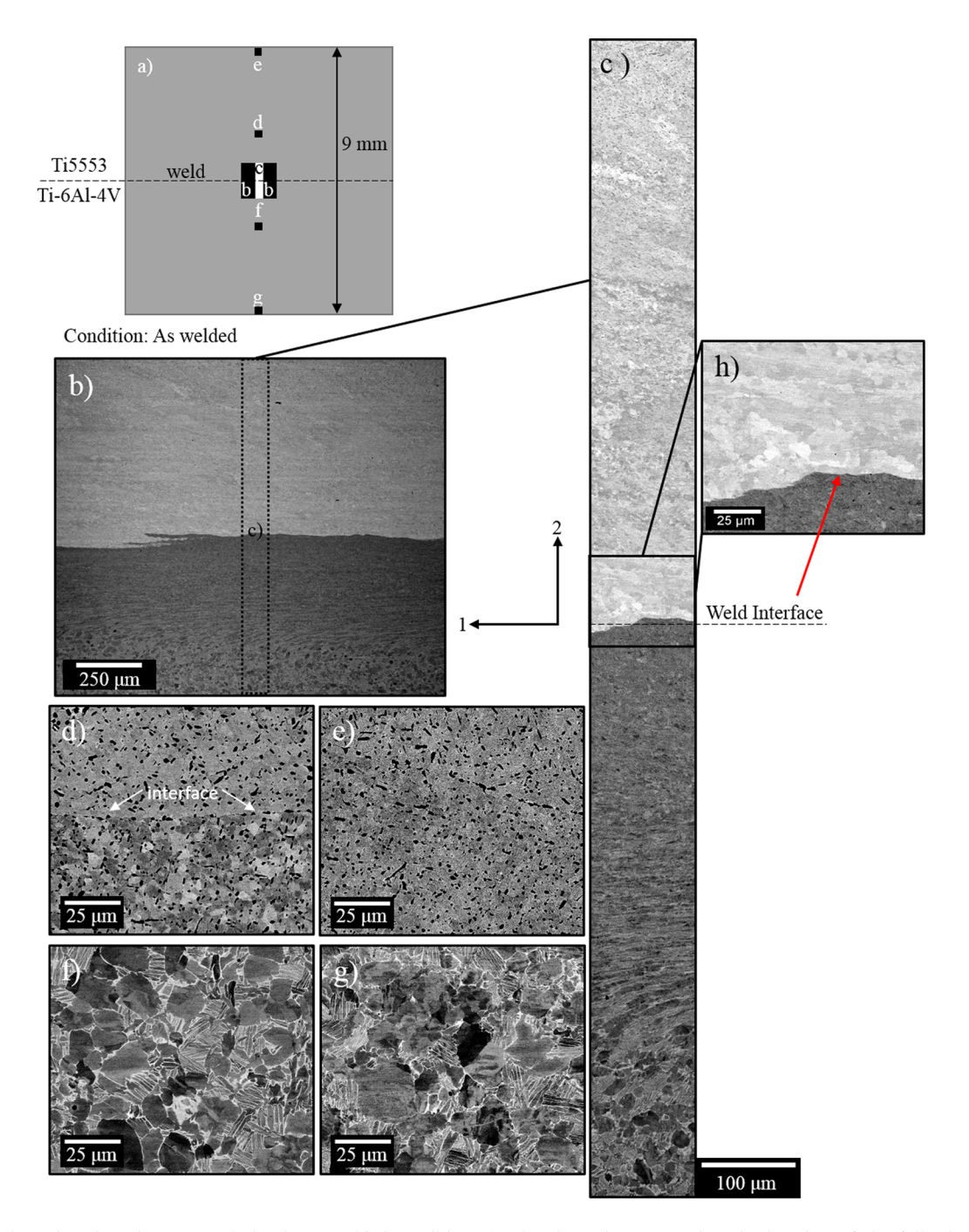


Fig. 13—Displays the Ti64-Ti5553 sample in the as-welded condition: (a) A schematic representing the location of the following images, in relation to the weld area, (b) an overview of the weld area, (c) an enlarged region, 1.23 mm in height taken across the weld region, approximately 0.6 mm in each direction, (d) a FOV 1.0 mm above the weld region, (e) a FOV 4.5 mm above the weld region, (f) a FOV 1 mm below the weld region, (g) a FOV 4.5 mm below the weld region, and (h) the weld interface created at the joining point of the two materials.

lamellar configuration with increased distance from the weld, as shown in Figure 13(g), located 4.5 mm from the weld interface. The weld interface, Figure 13(h), shows a fine basket-weave structure on the Ti64 side meeting the larger β grain structure in the Ti5553. The residual strain in the β phase is approximately four times than that in the α phase in the proximity of the weld interface, which is attributed to the choice of the second β peak during

peak fitting. This sample displays a tri-modal size distribution of α grains at distances greater than 1.5 mm from the weld interface in the Ti64 material, with only the fine basket-weave structure present at the weld interface, due to the rapid cooling after the weld process. A tri-modal size distribution of α grains was observed in the Ti64 side of the LFW sample, in which the α grains sizes are summarized in Table VI.

Table VI. Grain Size Measurements of Different α Grain Structures from the Ti64 Side of the LFW Ti64-Ti5553 AW Sample

	Ti64 Grain Size from LFW Ti64-Ti5553 AW					
	Distance from Weld	0 mm	1.5 mm	3.0 mm	4.5 mm	
α Grain size (μm)	Basket-weave thickness Lamellar thickness Globular	0.193 ± 0.08 N/A N/A	0.223 ± 0.11 1.02 ± 0.40 7.53 ± 3.2	0.229 ± 0.05 0.833 ± 0.35 8.27 ± 4.2	$0.288 \pm 0.09 \\ 1.03 \pm 0.45 \\ 7.06 \pm 3.0$	

The thickness or width of the basket-weave and lamellar structures are reported, and the average grain size of the globular α is reported using the line-intercept method to measure grain size.

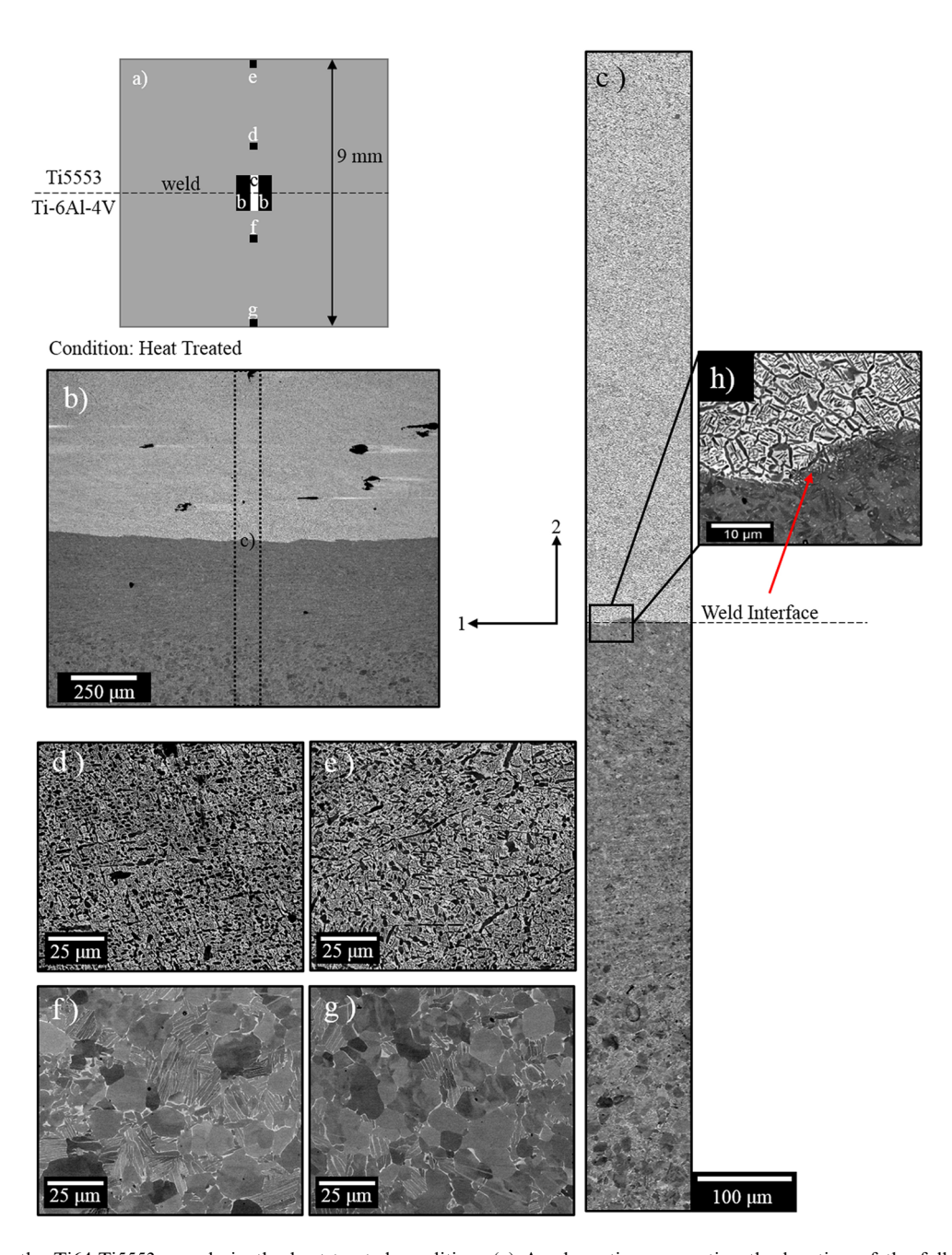


Fig. 14—Displays the Ti64-Ti5553 sample in the heat-treated condition: (a) A schematic representing the location of the following images, in relation to the weld area, (b) an overview of the weld area, (c) an enlarged region, 1.23 mm in height taken across the weld region, approximately 0.6 mm in each direction, (d) a FOV 1.0 mm above the weld region, (e) a FOV 4.5 mm above the weld region, (f) a FOV 1 mm below the weld region, (g) a FOV 4.5 mm below the weld region, and (h) the weld interface created at the joining point of the two materials.

Table VII. Grain Size Measurements of Different α Grain Structures from the Ti64 in the LFW Ti64-Ti5553 HT Sample

	Ti64 Grain Size from LFW Ti64-Ti5553 HT					
	Distance from Weld	0 mm	1.5 mm	3.0 mm	4.5 mm	
α Grain size (μm)	Basket-weave thickness Lamellar thickness Globular	0.327 ± 0.10 N/A N/A	0.353 ± 0.14 1.29 ± 0.41 10.99 ± 4.3	0.396 ± 0.10 1.24 ± 0.49 8.63 ± 3.8	$0.207 \pm 0.09 \\ 1.29 \pm 0.57 \\ 12.40 \pm 6.5$	

The thickness or width of the basket-weave and lamellar structures are reported, and the average grain size of the globular α is reported using the line-intercept method to measure grain size.

D. Ti64-Ti5553 LFW in the Heat-Treated Condition

Residual strain profiles in the α phase of the Ti64-Ti5553 HT sample are shown in Figure 9. The strain profiles show a flat and smooth behavior throughout the measured weld area. A similar trend is observed in the β phase (see Figure 10) except for a jump discontinuity in close proximity to the weld interface. Figure 14(a) is a schematic showing the location of the micrographs for the Ti64-Ti5553 sample in the heattreated condition. The weld region displays a variable microstructure with changing grain morphologies and size as distance is increased from the weld interface, along the 2 direction, as shown in Figure 14(b), with a magnified excerpt of this region shown in Figure 14(c). The grains are fully recrystallized, even in close proximity to the weld interface. This is consistent with the near-zero residual strain measured for ε_{11} and ε_{22} . The Ti5553 microstructure is shown in Figure 14(d), 1 mm and Figure 14(e), 4.5 mm from the weld interface. One notable difference between these two areas is that the α phase at a distance of 4.5 mm from the weld interface, Figure 14(e), is more interconnected, forming elongated structures instead of the equiaxed morphologies as seen more prominently 1 mm from the weld shown in Figure 14(d). On the Ti64 side of the weld, a similar trend in microstructure is observed at 1 mm, Figure 14(f) and 4.5 mm, Figure 14(g). In this case, the fraction of the α lamellar structures is decreasing with increased distance from the weld interface. Lastly, the weld interface, Figure 14(h), shows the fine basket-weave structure of the Ti64 intermingled with the α - β structure of the Ti5553. A tri-modal size distribution of α grains is observed in the Ti64 side of the weld; sizes are summarized in Table VII.

VI. CONCLUSIONS

In the present work, the residual strain distributions across the linear friction welded (LFW) joints of similar and dissimilar Ti alloys have been studied using energy-dispersive X-ray diffraction (EDD) method considering both the α and β phases and obtaining the five components (three axial and two shear) of the residual strain tensor. Key concluding remarks are summarized below.

• In-plane axial components of the residual strain tensor $(\varepsilon_{11}, \varepsilon_{22})$ show a symmetric behavior across

- the weld center in LFW joints of both similar and dissimilar Ti alloys. The post-weld heat treatment significantly reduced the residual strain in both samples.
- Strain distributions have been separately studied in the α and β phases. The residual strain in the β phase has been found to be significantly higher than that in the α phase, which can be attributed to differences in the stress state between the two phases, elastic stress anisotropy, morphologies of the two phases.
- Two jump discontinuities have been observed approximately at ± 1 mm from the weld center in the case of the LFW joint of dissimilar Ti alloys. This jump behavior has been partly explained via abrupt changes in the microstructural features at the respective locations. Such jumps in the HT sample also indicate different strain-free lattice parameters in the weld region as opposed to the parent materials, which was not accounted for in the present study. On the contrary, no such observation was made for the LFW joint of similar Ti alloys.
- A tri-modal distribution of the α phase grains was found in all specimens except the Ti64-Ti64 AW sample. Both AW conditions contained regions close to the weld that lacked a well-defined microstructure, upon heat treatment full recrystallization was observed in both the Ti64-Ti64 and Ti64-Ti5553 LFW samples. The Ti64-Ti64 sample in the HT condition contained finer grain sizes and lamellar α grains not present in the AW condition, while the Ti64-Ti5553 sample in the AW condition contained finer grains than that measured in the HT condition. All three configurations of α phase were present in both the AW and HT conditions of the dissimilar LFW samples.

ACKNOWLEDGMENTS

Financial support for this work was provided by the National Science Foundation (Grant Number CMMI 16-51956) under program manager, Dr. Alexis Lewis, and the Lightweight Innovation for Tomorrow Institute (Grant Number LIFT TMP-3a). Base materials for the Ti64-Ti64 and Ti64-Ti5553 welds were provided by Dr. Tom Broderick (GE) and Dr. Austin Mann (Boeing), respectively. The authors thank Dr.

Andrew Chuang (APS) for assistance with the setup of the EDD measurement. Use of the Advanced Photon Source was supported by the US Department of Energy, Office of Science, Office of Basic Energy Sciences, under Contract No. DE-AC02-06CH11357.

REFERENCES

- J. Cho, K. Conlon, and R. Reed: *Metall. Mater. Trans. A*, 2003, vol. 34A, pp. 2935–46.
- 2. I. Bhamji, M. Preuss, P.L. Threadgill, and A.C. Addison: *Mater. Sci. Technol.*, 2011, vol. 27, pp. 2–12.
- 3. R. Turner, R.M. Ward, R. March, and R.C. Reed: *Metall. Mater. Trans. B*, 2012, vol. 43B, pp. 186–97.
- 4. P.J. Withers: Rep. Prog. Phys., 2007, vol. 70, pp. 2211-64.
- P.J. Withers and H.K.D.H. Bhadeshia: *Mater. Sci. Technol.*, 2001, vol. 17, pp. 355–65.
- 6. V. Hauk: Structural and Residual Stress Analysis by Nondestructive Methods, Elsevier, Amsterdam, 1997.
- I.A. Denks, M. Klaus, and C. Genzel: *Mater. Sci. Forum*, 2006, vols. 524–525, pp. 37–44.
- 8. C. Genzel, I.A. Denks, R. Coelho, D. Thomas, R. Mainz, D. Apel, and M. Klaus: *J. Strain Anal. Eng. Des.*, 2011, vol. 46, pp. 615–25.
- W. Reimers, M. Broda, G. Brusch, D. Dantz, K.D. Liss, A. Pyzalla, T. Schmackers, and T. Tschentscher: *J. Non-Destructive Eval.*, 1998, vol. 17, pp. 129–40.
- A. Steuwer, J.R. Santisteban, M. Turski, P.J. Withers, and T. Buslaps: *J. Appl. Crystallogr.*, 2004, vol. 37, pp. 883–89.

- M. Croft, I. Zakharchenko, Z. Zhong, Y. Gurlak, J. Hastings, J. Hu, R. Holtz, M. Dasilva, and T. Tsakalakos: *J. Appl. Phys.*, 2002, vol. 92, pp. 578–86.
- 12. M.R. Daymond and N.W. Bonner: *Phys. B Condens. Matter*, 2003, vol. 325, pp. 130–37.
- M. Preuss, J. Quinta Da Fonseca, A. Steuwer, L. Wang, P.J. Withers, and S. Bray: J. Neutron Res., 2004, vol. 12, pp. 165–73.
- 14. J. Romero, M.M. Attallah, M. Preuss, M. Karadge, and S.E. Bray: *Acta Mater.*, 2009, vol. 57, pp. 5582–92.
- 15. P. Frankel, M. Preuss, A. Steuwer, P.J. Withers, and S. Bray: *Mater. Sci. Technol.*, 2009, vol. 25, pp. 640–50.
- P. Xie, H. Zhao, and Y. Liu: Sci. Technol. Weld. Join., 2016, vol. 21, pp. 351–57.
- SAE-AMS 4911H: SAE International, Warrendale, PA, USA, 1995, p. 1.
- 18. T. Ungár: Scr. Mater., 2004, vol. 51, pp. 777-81.
- 19. R. Young: Int. Union Crystallogr., 1993.
- 20. S.L.R. da Silva, L.O. Kerber, L. Amaral, and C.A. dos Santos: Surf. Coatings Technol., 1999, vols. 116–119, pp. 342–46.
- 21. M.B. Ivanov, S.S. Manokhin, Y.R. Kolobov, and D.A. Nechayenko: *Mater. Phys. Mech.*, 2010, vol. 10, pp. 62–71.
- 22. A.K. Śwarnakar, O. Van Der Biest, and B. Baufeld: *J. Alloys Compd.*, 2011, vol. 509, pp. 2723–28.
- 23. L. Thijs, F. Verhaeghe, T. Craeghs, J. Van Humbeeck, and J.P. Kruth: *Acta Mater.*, 2010, vol. 58, pp. 3303–12.
- J.V. Bernier, J.-S. Park, A.L. Pilchak, M.G. Glavicic, and M.P. Miller: Metall. Mater. Trans. A, 2008, vol. 39A, pp. 3120–33.
- M. Kasemer, R. Quey, and P. Dawson: J. Mech. Phys. Solids, 2017, vol. 103, pp. 179–98.
- 26. T. Ozturk and A.D. Rollett: Comput. Mech., 2017, pp. 1–16.
- K.M. Knowles and P.R. Howie: J. Elast., 2015, vol. 120, pp. 87–108.
- 28. D. Tromans: Int. J. Res. Rev. Appl. Sci., 2011, vol. 6, pp. 462–83.